PLOS BIOLOGY

RESEARCH ARTICLE

A critical-like collective state leads to long-range cell communication in *Dictyostelium discoideum* aggregation

Giovanna De Palo[1,2], Darvin Yi[3,4¤], Robert G. Endres[1,2]*

1 Department of Life Sciences, Imperial College London, London, United Kingdom, **2** Centre for Integrative Systems Biology and Bioinformatics, Imperial College London, London, United Kingdom, **3** Joseph Henry Laboratories of Physics, Princeton University, Princeton, New Jersey, United States of America, **4** Lewis Siegler Institute for Integrative Genomics, Princeton University, Princeton, New Jersey, United States of America

¤ Current address: Department of Radiology, School of Medicine, Stanford University, Stanford, California, United States of America
* r.endres@imperial.ac.uk

OPEN ACCESS

Citation: De Palo G, Yi D, Endres RG (2017) A critical-like collective state leads to long-range cell communication in *Dictyostelium discoideum* aggregation. PLoS Biol 15(4): e1002602. https://doi.org/10.1371/journal.pbio.1002602

Academic Editor: Robert H. Insall, CRUK Beatson Institute, UNITED KINGDOM

Received: September 30, 2016

Accepted: March 23, 2017

Published: April 19, 2017

Data Availability Statement: All relevant data are within the paper and its Supporting Information files.

Funding: GDP and RGE were supported by ERC Starting Grant 280492-PPHPI (https://erc.europa.eu/funding/starting-grants). The funders had no role in study design, data collection and analysis, decision to publish, or preparation of the manuscript.

Competing interests: The authors have declared that no competing interests exist.

Abstract

The transition from single-cell to multicellular behavior is important in early development but rarely studied. The starvation-induced aggregation of the social amoeba *Dictyostelium discoideum* into a multicellular slug is known to result from single-cell chemotaxis towards emitted pulses of cyclic adenosine monophosphate (cAMP). However, how exactly do transient, short-range chemical gradients lead to coherent collective movement at a macroscopic scale? Here, we developed a multiscale model verified by quantitative microscopy to describe behaviors ranging widely from chemotaxis and excitability of individual cells to aggregation of thousands of cells. To better understand the mechanism of long-range cell—cell communication and hence aggregation, we analyzed cell—cell correlations, showing evidence of self-organization at the onset of aggregation (as opposed to following a leader cell). Surprisingly, cell collectives, despite their finite size, show features of criticality known from phase transitions in physical systems. By comparing wild-type and mutant cells with impaired aggregation, we found the longest cell—cell communication distance in wild-type cells, suggesting that criticality provides an adaptive advantage and optimally sized aggregates for the dispersal of spores.

Author summary

Cells are often coupled to each other in cell collectives, such as aggregates during early development, tissues in the developed organism, and tumors in disease. How do cells communicate over macroscopic distances much larger than the typical cell—cell distance to decide how they should behave? Here, we developed a multiscale model of social amoeba, spanning behavior from individuals to thousands of cells. We show that local cell—cell coupling via secreted chemicals may be tuned to a critical value, resulting in emergent long-range communication and heightened sensitivity. Hence, these aggregates are

Abbreviations: ACA, adenylyl cyclase; c, connected; cAMP, cyclic adenosine monophosphate; CFP, cyan fluorescent protein; CI, chemotactic index; KS, Kolmogorov—Smirnov; LEGI, local excitation, global inhibition; ML, monolayer; nc, nonconnected; NN, nearest neighbor; PI3K, phosphoinositide 3-kinase; PKA, protein kinase A; WT, wild type.

remarkably similar to bacterial biofilms and neuronal networks, all communicating in a pulselike fashion. Similar organizing principles may also aid our understanding of the remarkable robustness in cancer development.

Introduction

Many living systems exhibit collective behavior, leading to beautiful patterns found in nature. Collective behavior is most obvious in animal groups with clear advantages in terms of mating, protection, foraging, and other decision-making processes [1, 2]. However, how cells form collectives without visual cues is less well understood [3]. There are two main strategies to achieve synchrony (or long-range order) among individuals: A leader (i.e., a special cell or an external chemical field) may influence the behavior of the others in a hierarchical fashion (top-down). An example is the developing fruit fly embryo in a maternally provided morphogen gradient [4, 5]. Alternatively, all individuals are equivalent and order emerges spontaneously by self-organization (bottom-up). Examples may include organoids [6] and other cell clusters [7], and both strategies are not mutually exclusive. While order itself cannot be used to differentiate between the two mechanisms, the response to perturbations or, simply, the correlations among fluctuations can be examined [8]. In top-down ordering, fluctuations are independent as cells follow the leader or the external field, and hence they are not influenced by their neighbors. In contrast, in bottom-up ordering, cells are coupled to their neighbors. Hence, fluctuations are correlated as neighboring cells influence each other [9]. Note that in this context, it is a reasonable assumption that cells can follow fluctuations of their neighbors much more easily than fluctuations of a distant leader cell. At a critical value of the cell—cell coupling strength, correlations may establish among cells that span the whole cell collective independent of its size, leading to a maximally connected collective similar to neurons in the brain [10].

To test these ideas of achieving order and long-range communication, we considered the well-known social amoeba *Dictyostelium discoideum*, which undergoes aggregation in response to starvation [11–13]. During this developmental process, cells start to secrete pulses of cyclic adenosine monophosphate (cAMP), a molecule that also acts as a chemoattractant for the other cells in the vicinity. The underlying signaling and regulatory pathways of such development have been thoroughly examined using genetics and imaging [14]: when a cell is "hit" by a high concentration of cAMP, it secretes a pulse of cAMP itself, relaying the signal and thus causing the formation of cAMP waves, which are inferred indirectly from optical density waves in dark-field movies [15, 16]. These waves propagate through the whole population [17–20]. As their development proceeds, cells pulse at higher frequencies, reaching frequencies of up to one pulse every 5 min in the aggregate [21, 22]. Cell movement also accompanies the secretion process: before cells start to secrete cAMP, they normally move incoherently; when cAMP waves form, cells move towards the direction of the incoming wave by following the cells emitting the pulse in an orderly fashion (streaming phase). Interestingly, in a microfluidic device, cells did not follow an artificially produced cAMP wave once it passed the cells, despite it producing a gradient behind the cells pointing in the opposite direction of cell movement. Hence, cells are thought to solve the so-called "back-of-the-wave" problem for directed unidirectional chemotaxis towards the aggregate [23, 24]. While single-cell chemotaxis [23–28] and large-scale pattern formation [16, 29–33] have been extensively studied, a precise characterization of the transition from single cells to multicellularity is still missing.

Here, we developed a multiscale model to capture the mechanism of aggregation, focusing on the distinction between induced and self-organized order. Specifically, we were able to

unify single-cell behavior and multicellularity at wide-ranging spatiotemporal scales. We achieved this by extending a single-cell model, which is able to describe *Dictyostelium* cell shape and behavior [25], by adding intracellular cAMP dynamics, secretion, and extracellular dynamics for cell—cell communication. To simulate hundreds of cells, we extracted a set of minimal rules for building a coarse-grained model. Hence, our approach is able to capture all stages of aggregation, ranging from single-cell chemotaxis to the multicellular collective. For quantifying the transition from disorder (preaggregate) to order (aggregate), we employed the mathematical concepts of spatial information and directional correlations. We found that the transition occurs during the streaming phase, which resembles a critical-like point known from phase transitions in physical systems as extracted by finite-size scaling. In physical systems, phase transitions are characterized by an abrupt change in the macroscopic properties of the system when an external parameter (such as temperature) crosses a well-defined value. In our cell system, this parameter is the cell density (or external cAMP concentration). Criticality was tested by corresponding analyses of previously recorded time-lapse movies from fluorescence microscopy (provided by the Gregor lab [22, 34, 35]). Comparison of different *Dictyostelium* strains showed that wild-type cells have a longer cell—cell communication range than any mutant strain with impaired aggregation (based on regA and rdeA mutant data from the Cox lab [21]), even if cells with enhanced cell—cell adhesion (such as cells that secrete less cell number "counting factor" [36]) form larger clusters. Hence, criticality may give cells an adaptive advantage, leading to optimally sized aggregates.

Results

A single-cell model fulfills criteria for aggregation

To model the transition from single cells to multicellularity, we started with cell shape and behavior in single cells. Specifically, we considered a model capturing single-cell membrane dynamics similar to the Meinhardt model [25, 26, 37]. Although not based on specific molecular species, this model describes membrane protrusions (such as pseudopods) and retractions as well as resulting cell movement by means of three effective equations (see Supporting information). The first and second variables are a local activator and a global inhibitor (both are also considered in the local excitation, global inhibition [LEGI] model [27, 28]). The third is a local inhibitor, which is important in order to destabilize the current pseudopod and to increase the responsiveness of the cell (Fig 1A, left). To this we added equations representing the internal cAMP dynamics based on the FitzHugh—Nagumo model (Fig 1A, middle) [34, 35]. These are meant to capture the intracellular cAMP dynamics that are governed by the relative activities of adenylyl cyclase (ACA), which synthesizes cAMP, and 3′,5′-cyclic-nucleotide phosphodiesterase regA, which degrades cAMP. Based on experimental evidence, we assumed that cAMP is released from the rear of the cell [38, 39]. We also modeled extracellular cAMP dynamics for cell—cell communication, taking into account diffusion of cAMP in the extracellular medium and its degradation by secreted phosphodiesterase PDE (Fig 1A, right; see Materials and methods for further information and Supporting information for numerical implementation).

Using this detailed model, we investigated the behavior resulting from cell—cell interactions in very small systems. First, we wanted our model to capture streaming (i.e., the ability of a cell to precisely follow the cell in front of it). To reproduce that, we simulated a single cell in a rectangular box with periodic boundary conditions (see Fig 1B and S1 Movie). In mathematics, periodic boundary conditions mean that the box is neighbored by identical copies of the box. Thus, in practice, if a cell passes through one side of the box, it reappears on the opposite side with the same velocity. This effect also applies to the molecules surrounding the cell. Now,

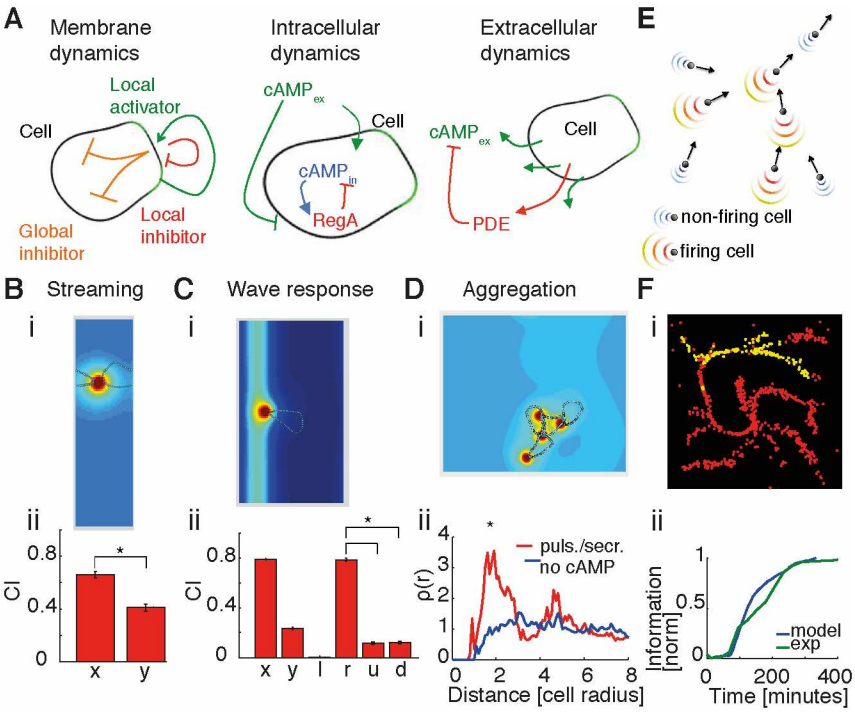

Fig 1. Multiscale model: From single cell—shape changes and chemotaxis to collective behavior. (A) Schematics for membrane dynamics (left), intracellular cyclic adenosine monophosphate (cAMP) dynamics (center), and extracellular cAMP dynamics (right). (B) Single-cell "streaming" simulation in a box with periodic boundary conditions and a constant concentration of cAMP (i). Box dimensions are about 25 x 90 μm (the initial cell radius is assumed to be ∼15μm). Because of the small dimension of the box, the cell is just leaking, not pulsing, in order to avoid saturation of secreted cAMP. The simulation was repeated 12 times, and the average chemotactic index (CI) was calculated (ii). Error bars represent standard errors. Differences in CI_x and CI_y are statistically significant ($p < 0.01$), using a Kolmogorov—Smirnov test (KS test). (C) Cells solve "back-of-the-wave" problem. (i) A Gaussian wave ($\sigma^2 \sim 60\mu m$) moves from right to left with a speed of about 300 μm/min [40]. At the peak of the wave, the cell emits a pulse of cAMP. After the firing, the cell enters a refractory period during which it can neither fire again nor repolarize. The cell generally moves to the right and hence does not follow the passing wave. (ii) CI in *x* and *y* as well as in left (negative *x*), right (positive *x*), up (positive *y*), and down (negative *y*) directions in order to discriminate between the directions of the incoming (right direction) and outgoing (left direction) wave. Simulations are repeated 12 times; shown are averages and standard errors. Box is about 60 x 105μm. CI in the right direction is significantly higher than CI in the other directions. (D) "Aggregation simulation." (i) Four cells are simulated moving in a constant concentration of cAMP. At the beginning, cells are randomly distributed. (ii) Density correlation at the end of simulations is plotted for control cells without secretion (blue) and all cells leaking cAMP and one cell also emitting pulses of cAMP (red). The red line has a significant ($p < 0.05$, KS test) peak at a distance of about two cell radii, representing cell—cell contact. Simulations in this case are also repeated 12 times. Box dimensions are 75 x 75 μm. See Materials and methods for details on density correlation, Supporting information for a full explanation of the detailed model, and S1 and S2 Data for data and code from simulations, respectively. (E) Schematic showing cells represented as point-like objects with velocity vectors. Firing cells emit pulses of cAMP, and nonfiring cells secrete cAMP at a low constant leakage rate. Spatial cAMP profiles are derived from detailed model simulations. At every time point, cells are allowed two possible directions of movement in order to reproduce pseudopod formation at the cell front, with directions changing by ±27.5˚ with respect to the previous movement, corresponding to an angle between pseudopods of about 55˚ [41]. (F) Screenshot during streaming for $n = 1{,}000$ simulated cells (i). Red (yellow) points represent nonfiring (firing) cells. (ii) Spatial information versus time: simulations (blue) compared with experimental dataset 3 (green). Values were then normalized and shifted in time to facilitate comparison; see S3 Data for the numerical values.

https://doi.org/10.1371/journal.pbio.1002602.g001

given the rectangular shape of the box with the long side in the vertical direction and the short side in the horizontal direction, a horizontally moving cell can sense its own secretion (as the box is neighbored by identical copies of the box and hence copies of the cell and cAMP). Hence, the front of the cell is able to sense the secreted cAMP at the rear of the neighboring

cell. In contrast, a vertically moving cell is too far away from its rear and thus cannot sense its secretion. We estimated the ability of the cell to stream by measuring the chemotactic index (CI) in the *x* direction, calculated as the amount of movement in the horizontal direction compared to the total length of the trajectory. In Fig 1B, we show that the CI in the *x* direction is significantly higher than the CI in the *y* direction.

We then considered the wave response as measured in microfluidic experiments, in which cells are exposed to traveling waves of cAMP [23, 24]. When hit by a traveling wave, cells moved towards the direction of the incoming wave but did not follow the wave after it passed. In order to capture this robust chemotaxis behavior, our model cell undergoes a refractory period (as was done in previous models [29, 31]) during which the cell can neither repolarize nor pulse (see Supporting information for further details). Experimental evidence for this refractory period stems from the several-minute-long directional bias in cell polarization [42] —which may be caused by the large-scale inert cortical structure or phosphoinositide 3-kinase (PI3K)—that stays on the membrane even when no longer active [43]. In our simulations, this refractory state is naturally achieved when the cell spontaneously emits a pulse of cAMP upon encountering the wave (see Fig 1C and S2 Movie). As a result, the CI is significantly higher in the right direction of the incoming wave. Finally, we considered a small number (four) of cells in a small box (with periodic boundary conditions) and tested whether they showed signs of aggregation (see Fig 1D and S3 Movie). Specifically, we measured the tendency of the cells to cluster by calculating the density pair correlation function (see Materials and methods) and compared the cases with and without secretion of cAMP. In the absence of secretion, cells were randomly distributed in space at the end of the simulations, as evident by the relatively flat horizontal line of unit correlation for distances larger than one cell length (the reduction at close distance is due to volume exclusion). With secretion, cells tended to be much closer to each other, with a clear peak in the density distribution at cell—cell contact (distance of two cell radii), indicating that cells tend to be close to each other and hence to cluster.

A coarse-grained model reproduces collective behavior

In order to reproduce aggregation as observed in experiments (e.g., [22, 34]), we needed to simulate hundreds to thousands of cells. However, the detailed model introduced in the previous section is computationally too expensive, forcing us to introduce several simplifications. In our coarse-grained simulations, cells are point-like objects moving in continuous space. In particular, we took advantage of the spatiotemporal cAMP profiles from the detailed model by extracting the concentrations typically secreted by a single cell during leakage or a pulse. Shaped by degradation and diffusion, these profiles are approximately short-ranged exponential with a decaying amplitude in time. To capture the effects of volume exclusion, we also reduced the gradients in the cell-forward direction (see Materials and methods for further information). Hence, as in the detailed model, the maximum cAMP concentration secreted by an individual cell is always found in the direction opposite to the direction of its motion. Using these analytical cAMP profiles, the cAMP concentration a cell senses is given by the sum of secretions by its neighboring cells. We then set concentration and gradient thresholds to determine whether a cell leaks or pulses cAMP, followed by a refractory period, and whether a cell moves randomly or follows the local cAMP gradient (see Fig 1E, Materials and methods, and Supporting information for a detailed explanation of the model).

Using this minimal set of rules, we simulated thousands of cells with a density similar to the experimental ones (around a monolayer [ML] with 1 ML = 6,600 cells/mm^2 [22, 34]). Cells were initially distributed uniformly in space and allowed to move randomly. As soon as the cell density (and hence local cAMP concentration) increased spontaneously because of

random cell motion, a cell may sense a concentration of cAMP large enough to pulse, and this excitation will propagate throughout the whole population. Because of cell movement, streaming and aggregation into a small number of clusters can be observed (Fig 1F and S4 Movie). To quantify aggregation in a mathematical way, we estimated the "degree of order" (or spatial information) in an image. This spatial information is based on the calculation of the 2-D Shannon entropy, which does not require tracking of individual cells (see Materials and methods for mathematical details and Supporting information for a primer on information theory) [44]. In this framework, evenly distributed cells correspond to a low spatial information, while highly clustered cells have a high spatial information. In all simulations, we observed that the spatial information rises sharply during the streaming phase as expected for cells in an ordered aggregate (see Fig 1F). Interestingly, the spatial information was previously used to capture the second-order (disorder—order) phase transition in the 2-D Ising model (magnetic spins on a lattice) [44]. Hence, we wondered whether aggregation may be viewed as a critical-like point that describes the sudden transition from individual cells to the cell collective?

Collective behavior: Hierarchical or self-organized?

Based on our model assumptions, all cells are treated the same. However, aggregation may still be driven by the first random cell pulsing (hierarchical system) or can spontaneously emerge as cells are coupled to each other by cAMP sensing and secretion (self-organized system; Fig 2A). The order of the collective process can be measured by studying the directional correlations of pairs of cells. Specifically, the nonconnected (nc) correlations

$$C_{nc}(r) = \frac{\sum_{i \neq j}^{N} \overrightarrow{u_i} \cdot \overrightarrow{u_j} \delta(r - r_{ij})}{\sum_{i \neq j}^{N} \delta(r - r_{ij})} \quad (1)$$

represent the average similarity of the direction of motion for every pair of cells depending on their distance, where N is the total number of cells, $\vec{u}_i$ is the vector representing the direction of cell i, and $\delta(r - r_{ij})$ is equal to 1 if $r = r_{ij}$ and 0 otherwise. $C_{nc}(r)$ also represents the order parameter in our system (i.e., the quantity describing the degree of order or polarization in the system). For instance, when cells move independently of each other in random directions, then the order parameter is zero. In contrast, when all cells move in the same direction, then the order parameter would be maximal (i.e., one). By calculating this quantity for every time frame, we were able to analyze its variation in time. During the preaggregation stage, correlations are close to zero even at short distances, while they increase sharply during the streaming phase (Fig 2B, top).

Although order increases during the streaming phase, the origin and characteristics of this order are yet to be determined. To achieve this, we need to know more than the fact that the directions of cell movement are correlated (which describes the degree of order even in a hierarchical, top-down system). In addition, we also need to know if the fluctuations of the directions are correlated. This would describe to what level cells communicate with each other and how they would respond collectively to perturbations.

For this purpose, we calculated the connected (c) directional correlations $C_c(r)$, measuring the similarity of the directional fluctuations with respect to the average velocity [8, 9]. For instance, $C_c = 0$ ($C_c = 1$) means that a change in a cell's direction is independent of (perfectly matched by) changes in the direction of its surrounding cells. To obtain the connected correlations, direction $\vec{u}_i$ in Eq 1 is substituted by the velocity of the single cell when the average is subtracted: i.e.,

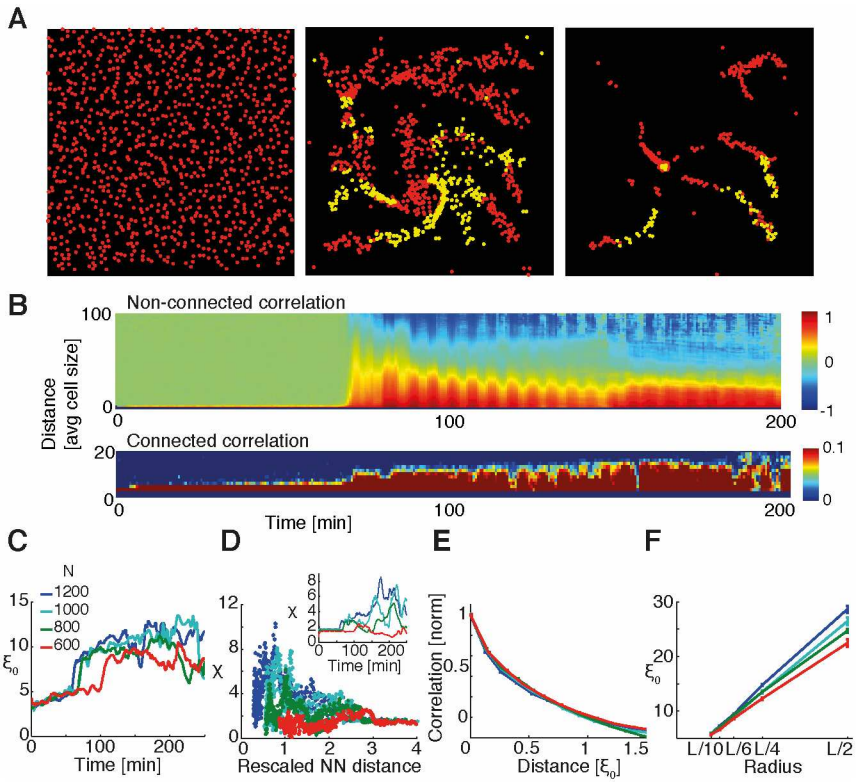

Fig 2. Coarse-grained model leads to collective behavior. (A) Screenshot of simulation for $n = 1{,}000$ cells at different time points: prestreaming (left), streaming (center), and after aggregation (right). Red (yellow) points represent nonfiring (firing) cells. See Supporting information for the full movie. (B) Kymograph of nonconnected C_{nc} and connected C_c directional correlations for simulation of $n = 1{,}000$ cells. Directional correlation profiles $C(r)$ were calculated for every time frame and displayed depending on distance r. For cell size, we used the volume exclusion length of 3 μm. (see Materials and methods). (C) Correlation length versus time for different numbers of cells ($n = 1{,}200$, 1,000, 800, and 600). Data were smoothed with a moving average filter spanning ten consecutive frames. (D) Susceptibility χ plotted with respect to nearest-neighbor (NN) distance for different numbers of cells and with respect to time (inset). Nearest-neighbor distance was rescaled by the volume exclusion length (see Materials and methods). The peak in susceptibility becomes higher the larger the number of cells, and NN distances decrease accordingly. Profiles in the inset were smoothed with a moving average filter spanning ten points. (E) Comparison of correlation profiles for streaming phase (50-min time window). Connected correlations, calculated for different numbers of cells and normalized so that the correlation length was equal to one, were plotted as a function of distance in units of their respective correlation lengths. The four profiles collapse onto a single curve, independently of the number of cells. (F) Average correlation length versus neighborhood radius for different numbers of simulated cells. L corresponds to the size of the images (389 μm). ξ_0 represents the average correlation length during streaming phase (50-min window). Error bars represent standard errors. See Supporting information for a full explanation of the model and S4 and S5 Data for MATLAB code and data, respectively.

https://doi.org/10.1371/journal.pbio.1002602.g002

$\delta\vec{u}_i = \delta\vec{v}_i / \sqrt{\frac{1}{N}\sum_{j=1}^{N}\delta\vec{v}_j^2}$ with $\delta\vec{v}_i = \vec{v}_i - \frac{1}{N}\sum_{j=1}^{N}\vec{v}_j$. For this kind of collective movement, such a subtraction is not straightforward. If we compute a global average velocity for every time frame, we systematically overestimate the nonconnected correlations because we still consider part of the "bulk" velocity vectors as a result of the position of the cells in the image (see Supporting information for a schematic explanation). To reduce this artefact, we considered local averages. For every cell, we considered the average velocity of all cells in its neighborhood up to a certain maximal distance r_c, computed the correlations between the cell in the center and all the cells belonging to its neighborhood, and repeated this procedure for every cell in our image.

When applied to the simulations, Fig 2B, bottom shows significant connected correlations, especially during streaming. Next, we considered the correlation length ξ_0 (i.e., a cell's "influence radius" over its surrounding cells). We estimated this correlation length by the minimum distance at which the correlations cross zero, i.e., $C(r = \xi_0) = 0$ [8]. We found that ξ_0 is indeed much larger than the minimum nearest-neighbor distance. This indicates that a cell influences other cells way beyond its immediate neighbors, strongly suggesting self-organization (Fig 2C).

Streaming as a critical-like point

Above, we demonstrated that aggregation in *Dictyostelium* is highly ordered and self-organized, with a correlation length much greater than the nearest-neighbor distance. Does the transition from disorder to order in this finite system show signs of criticality, given by a drastic and sudden qualitative change in behavior? At criticality, all cells would remarkably influence each other independent of the distance between them.

In order to answer this question, we considered that in critical systems, the correlation length should scale with the size of the system as there is no intrinsic length scale [8]. To investigate this, we analyzed how the correlation length ξ_0 changes in time. In all simulations, ξ_0 was small before aggregation and increased markedly during the streaming phase (Fig 2C). In equilibrium phase transitions, the susceptibility describes how sensitive the system is to perturbations, and this quantity would diverge at the critical point for an infinitely large system. Thus, this divergence indicates that the whole (infinite) system responds coherently as a single unit. In our cell system, the susceptibility can approximately be computed by the integrated correlations (i.e., by the amount of correlated cells),

$$\chi = \frac{1}{N}\sum_{i\neq j}^{N} \delta\vec{u_i} \cdot \delta\vec{u_j}\theta(\xi_0 - r_{ij}), \tag{2}$$

where $\theta(\xi_0 - r_{ij})$ is equal to 1 for $r_{ij} < \xi_0$ and 0 otherwise [8]. This proxy for the susceptibility peaks precisely during the streaming phase (Fig 2D, inset), and the higher the number of cells, the higher the susceptibility. Moreover, if we consider cell density as a control parameter (similar to temperature or coupling in a ferromagnetic Ising model), we can plot χ with respect to the rescaled nearest-neighbor distance (Fig 2D and Materials and methods). The resulting peak heights do not only reflect the number of cells, but their positions also shift to smaller nearest-neighbor distances (i.e., cells become more densely packed) as the number of cells increases, further supporting the resemblance to a scale-free system near criticality [8]. In theory, this peak height should keep increasing with cell number and ultimately diverge at a critical nearest-neighbor distance for an infinite system. Furthermore, by normalizing the correlations (so that they are one at the start for small distances) and rescaling the distance by the correlation length, the correlations collapse for all our simulations (Fig 2E). This collapse of the curves shows that they all have the same shape upon rescaling, indicating self-similarity as often occurs at criticality [45]. Finally, we took advantage of our image partition with different radii r_c to examine how the correlation length ξ_0 scales with system size. We noticed that for all movies, higher cell numbers display longer correlation lengths for a given neighborhood radius and that the correlation length increases with increasing radius. Hence, the correlation length scales with system size (Fig 2F), indicating critical-like behavior in our simulated cells.

Analysis of time-lapse fluorescent microscopy

To test the model, we analyzed five previously recorded movies of *Dictyostelium* aggregation with different cell densities from [22, 34] (see Materials and methods and S5 Movie). Briefly,

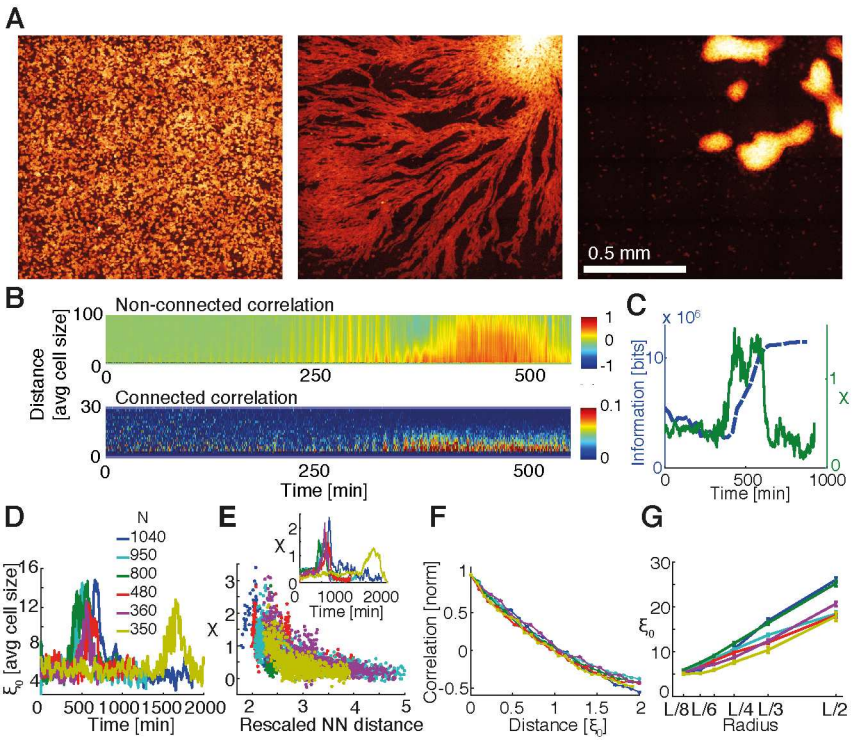

Fig 3. Collective behavior in experimental data for validating model. (A) Cyan fluorescent protein (CFP) images of *Dictyostelium* aggregation of dataset 3. Images were taken after 4–5 h of starvation, when cells were still moving randomly, before initiating aggregation (left), during streaming phase (450 min after first image, center), and after aggregation (800 min, right). (B) Kymograph of nonconnected C_{nc} and connected C_c directional correlations for the movie in dataset 3. Distance r is expressed in units of average cell size (estimated after an ellipse was fitted to every cell contour and corresponding to the average of the minor axis, ~10.7 μm). (C) Spatial information (blue) and susceptibility χ (green) of movie in dataset 3 as a function of time. The increase in spatial information denoting a more ordered image corresponds to the peak in susceptibility. (D) Correlation length ξ_0 as a function of time for the six movies. Curves were smoothed with a moving average operation spanning 20 time points for better visualization. Inset: comparison of cell number estimated from TRED images during the streaming phase for different movies. (E) Susceptibility χ as a function of rescaled nearest-neighbor (NN) distance and as a function of time (inset). Note that the height of peaks increases and that the corresponding rescaled NN distance decreases with the number of cells, as it does for simulations. Rescaled NN distance was computed by normalizing NN distance by the average cell size. In order to decrease noise, profiles in the inset were smoothed with a moving average spanning 20 time points. (F) Normalized C_c as a function of correlation lengths ξ_0 for different movies. C_c for every dataset was calculated as an average over 150 min of the streaming phase. Error bars represent standard errors. Similar to the simulated data, curves collapse for different numbers of cells when correlations are plotted as a function of distance in units of their respective correlation lengths. (G) Average correlation length versus neighborhood radius. L corresponds to the size of images (2,033 pixels, ~1.3 mm). ξ_0 represents the average of 150 min during the streaming phase. Error bars represent standard errors. Cell positions and tracking for the different experimental data are provided in S6–S11 Data, with actual data provided in S12 Data. Numerical results for the correlation analysis for panels D–F are provided in S13 Data and for panel G in S14 Data.

https://doi.org/10.1371/journal.pbio.1002602.g003

during 15 h of observation, individual cells become a single, multicellular organism, going through different stages including preaggregation, streaming, and aggregation (see Fig 3A). Cell densities ranged from 1/3 ML to almost 1 ML, ensuring aggregation while restricting our system to 2-D. A 10% subpopulation of cells expressing the mRFPmars (also known as TRED) fluorescent marker were tracked using a custom-written software (see Materials and methods). Based on these cells, we repeated the analysis from the simulated cells for the TRED cells from the experiments, applying spatial information, nonconnected and connected correlations, correlation length, and susceptibility. As we used the same computational protocol for both

simulations and data, a close comparison was possible, which allowed us to assess finite-size scaling and hence critical-like behavior.

Based on our analysis of the data, the correlation length ξ_0 increases during the streaming phase, as does the susceptibility χ (Fig 3B–3E). Additionally, χ increases with cell number (and hence cell density), and the nearest-neighbor distance decreases, similar to the simulations. The correlation profiles, normalized and rescaled by the nearest-neighbor distance, largely superimpose for the different cell numbers, indicating that the slope of the resulting curves is not affected by the number of cells (see Fig 3F). Note that the cell density changes slightly over the duration of observation because of open boundary conditions (the observation field is smaller than the field of cells so cells can freely move in and out of the observation field; see Supporting information for a quantification). Hence, cell numbers reported refer to the streaming phase (Fig 3D, inset). Finally, we studied how the correlation length changes for different system sizes by considering different neighborhood radii as performed for the simulations (see Materials and methods). We noticed that ξ_0 increases for a given radius with increasing cell numbers and also for a fixed number of cells with increasing neighborhood radius (Fig 3G). These observations strongly suggest that there is no intrinsic correlation length but that this length scales with system size. Taken together, our results suggest that aggregation can be viewed as a critical-like point in this finite system.

Wild-type cells are better at long-distance cell communication than aggregation-impaired mutant cells

While criticality leads to long-range cell—cell communication, what is its biological function in aggregation and ultimate spore dispersal? This question can also be raised from the perspective of modeling: many published models achieve aggregation [29, 31, 46] (although assessing potential differences in the quality of aggregation is difficult in retrospect). If aggregation is readily achievable, what does criticality add to aggregation? There might be two ways to interpret this paradox: One is that all successful models are fine-tuned to achieve aggregation, and this special point is again our critical-like point. Alternatively, simple aggregation is easy to achieve, but aggregation of thousands of cells into a single aggregate (or very few aggregates) is difficult and requires a diverging correlation length and hence exceptionally good long-range cell—cell communication. In this context, criticality may help to make this process robust to variability and obstacles in nature, as often microscopic details do not matter near a critical point [47–49].

To address this important question, we altered model parameters or reduced earlier assumptions. Specifically, we conducted aggregation simulations of 500 cells with (1) uniform (radially symmetric) secretion of cAMP (instead of secretion from the cell rear); (2) increased sensing noise (to address the naturally occurring cell-to-cell variability); (3) additional cell—cell adhesion (by the TgrA/C adhesion system during late aggregation [50]), which was not part of our original model; and (4) mutant cells with asynchronized cAMP secretion (similar to the regA mutant [22]). Experimentally, it was found that regA and rdeA with a diminished phosphorelay ability as well as PDE mutants are able to aggregate, albeit into smaller clusters without streaming [51–55]. Furthermore, mutants with decreased "counting factor" secretion (countin, cf45-1, cf50, or cf60) and hence increased cell—cell adhesion form larger cell clumps [36, 54, 56]. These cell types are implemented in our simulations as described in the Supporting information.

To quantify the range of cell—cell communication and the quality of aggregation, we considered the correlation length during the streaming stage and the spatial information of the final aggregate, respectively. Fig 4, panels A and C show that these additional modified

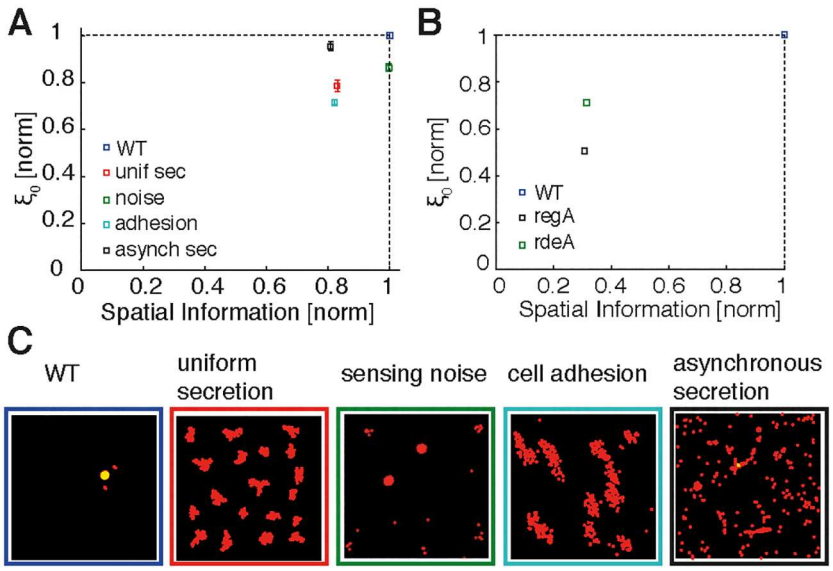

Fig 4. Role of criticality in aggregation of wild-type and mutant cells. (A) Correlation length (during streaming) and spatial information (of final aggregate) for coarse-grained simulations of $n = 500$ cells for wild-type (WT) and modified cell types. Correlation length and spatial information are normalized with respect to WT (blue symbol). Modified-cell simulations were performed with uniform (radially symmetric) secretion of cyclic adenosine monophosphate (cAMP) (red), significantly increased sensing noise (10-fold increase in standard deviation compared to WT noise; green), enhanced cell—cell adhesion (light blue), and asynchronized secretion (random pulsing; black). (B) Corresponding correlation length and spatial information for experimental data from Fig 5 of [55], considering WT cells (blue) and protein kinase A (PKA) pathway mutants (with the asynchronous regA mutant in black and the phosphorelay intermediate protein [rdeA] mutant in green). (C) Screenshots show cell distributions at the end of the simulations from (A). Error bars represent standard errors in correlation length for an average in time of 50 min during the streaming stage. See Supporting information for a detailed explanation and S15 and S16 Data for numerical values for simulations and experimental data, respectively.

https://doi.org/10.1371/journal.pbio.1002602.g004

simulations exhibit decreased correlation lengths and spatial information as compared to our previous simulations (wild-type cells). Surprisingly, this even applies to the simulations with enhanced cell—cell adhesion, which produce broader aggregates as compared to wild-type cells. Thus, strong cell—cell adhesion leads to strong order, but apparently this does not allow for sufficient flexibility during the aggregation process. These findings are not in contradiction to earlier modeling, in which uniform secretion and adhesion allowed streaming to occur [57]; our results simply show that secretion from the cell rear further improves long-range cell communication and cell streaming and that early adhesion can be detrimental to streaming. Subsequently, we estimated the correlation length and spatial information from previously published movies of wild-type cells as well as regA and rdeA mutants [21, 55] (for details, see Supporting information). Similar to our simulations, we found that also in experiments wild-type cells have a larger correlation length and spatial information than any of the analyzed mutants (Fig 4B). Note that the simulations with "sensing noise" and "asynchronous secretion" can be made even noisier, which would reduce the correlation length and spatial information even further to match the data better.

Hence, criticality may allow wild-type cells to create aggregates of just the right size and, we speculate, may also be useful for decision making on where to aggregate as well as for increased robustness in the presence of obstacles and cell-to-cell variability. For instance, if aggregates are too small, stalks may be too short to disperse spores efficiently or too thin to support the weight of the spores [54]. In contrast, if aggregates are too large, then cells may encounter

difficulties in decision making or cell sorting, or their stalks may collapse under the weight of too many spores. Hence, criticality may allow cells to make informed decisions for achieving optimal aggregate sizes for the most effective spore dispersal. This would indicate that criticality constitutes an adaptive advantage.

Discussion

Dictyostelium aggregation represents a fascinating example of synchronous collective cell behavior, spanning ~ 1 mm in length although cells are just ~ 10 μm in size. Here, we asked how cells achieve such exquisite long-range communication [58], when the transition from single cells to the a collective occurs, and how this transition can be characterized quantitatively. To capture the main features of aggregation, we developed a multiscale model. First, we focused on single cells using a detailed model combining sensing, cell-shape changes, and movement with cAMP secretion or pulsing and hence cell—cell communication. Once this model resembled the behavior of a single cell or a small group of cells, it allowed us to extract a minimal set of rules that could lead to aggregation. In particular, we extracted the cAMP concentration profile of a pulse from the detailed simulations and the refractory period after pulsing. By allowing cells to leak cAMP and to randomly move below a certain cAMP threshold concentration, we were able to observe spontaneous random pulsing as soon as the local density increased, similar to what occurs in real cells. This minimal set was subsequently included in the coarse-grained agent-based model, which is able to reproduce the collective behavior of hundreds of cells in line with time-lapse microscopy [22, 34].

Our major findings point towards previously uncharacterized features in aggregation, both observable in simulations and data. First, the transition to the collective is exactly pinpointed by a sharp rise in the spatial information of the cells during streaming. Second, to quantify the nature of the transition, we used fluctuations around the mean velocity, allowing us to distinguish between a hierarchically driven, top-down (external gradient from leader cells) and an emergent, self-organized, bottom-up (all cells are equal) process. Third, similar to second-order phase transitions in physical systems, the streaming phase shows signatures of criticality using finite-size scaling arguments. As a result, there is no intrinsic length scale, allowing cells to communicate with each other over large distances "for free" (i.e., only based on local cell—cell coupling). The control parameter is cell density, affecting the cell—cell coupling via cAMP secretion and sensing.

Our work provides further insights into the process of cell aggregation. By means of our multiscale model, we were able to answer why cells emit cAMP in pulses. Albeit short lived, a pulse creates a steeper spatial cAMP gradient than continuous secretion (assuming that the total amount of emitted cAMP is the same in both cases). Moreover, we noticed that so-called cAMP "waves" are likely not actual macroscopic traveling waves because of strong dissipation and diffusion. In contrast, cells are exposed to short-range cAMP pulses, which need to be relayed from one cell to the next before they dissipate. Although cAMP waves from microfluidic devices were used to study the cellular response to positive (incoming wave) and negative (passing wave) gradients, they may not represent natural stimuli [23, 24]. Hence, cells may not have to solve the traditional "back-of-the-wave" problem but instead have to decide which pulse to follow. However, this difficulty is eased as cells secrete cAMP from their rear [39]. Indeed, experiments of constitutively expressed adenylyl cyclase show defective streaming [59].

Our multiscale model captures true emergence, which is generally not included in previous models of *Dictyostelium* aggregation. Models of wave propagation and spiral wave patterns go back as early as the 1970s [60], but generally these models did not include cell motility (but see

[61] for an exception). More elaborate models from the 1990s focused on actual aggregation [16, 20, 29–31, 46]. These were followed by the biologically more detailed LEGI [27, 28] and Meinhardt [26, 37] models to address the single-cell response to chemoattractant gradients. More recently, the FitzHugh—Nagumo model was adopted to explain the pulsing and synchronization of multiple cells (see Supporting information for a comparison) [34, 35], although early attempts to understand cAMP oscillations and the signal relay were already conducted in the 1980s [20]. Furthermore, hybrid models were proposed [62]. However, none of these models started from a detailed, spatiotemporal, single-cell model and was able to quantify the cell—cell correlations, type of order, and exact transition point for achieving collective behavior.

When dealing with complex biological phenomena, there are necessarily limitations in the deduced models and acquired data. To assess criticality via finite-size scaling, ideally cell density is varied by orders of magnitude. However, this is often difficult to achieve in biological systems and depends on experimental conditions. On the one hand, if cell density is much lower than about 1/3 ML, cells do not aggregate [34] (although lower density aggregation was achieved in a different experimental setup [63]). On the other hand, if the cell density is higher than 1 ML, experiments would need to be conducted in 3-D with major technical difficulties. Despite the approximations, our model allows the identification of the key ingredients for certain observed behavior. For instance, an earlier version of our model showed some level of aggregation but no finite-size scaling. By investigating this shortcoming, we noticed that streams were too narrow because of nearly negligible volume exclusion. However, quasi—one-dimensional streams restrict cell movement and suppress criticality, reminiscent of the missing disorder—order phase transition in the 1-D Ising model according to the Mermin—Wagner theorem [64]. (Note that the 2-D Ising model is a borderline case, but it is still possible to formally define a phase transition according to Kosterlitz and Thouless [65].) In our simulations, only when volume exclusion is increased and streams become broader does critical-like behavior emerge (see also Discussion in [47]).

In an attempt to unify wide ranging biological phenomena, short-range interactions may play similar roles in cell collectives (*Dictyostelium*, neurons, biofilms, embryos, tumors) [10, 66, 67] and animal groups (such as bird flocks) [8, 9, 68–70]. Interestingly, many different cell types communicate by pulsing (spiking), including neurons and bacteria [71]. Operating at criticality (i.e., the tipping point between order and disorder) may allow cells to be maximally responsive; to communicate robustly over long distances; to act as a single, coherent unit; and to make decisions on, e.g., when and where to aggregate. In the future, it would be fascinating to conduct aggregation experiments in 3-D environments and to study the collective response to perturbations such as obstacles, changes in temperature, and exposure to toxins.

Materials and methods

Detailed model

The intracellular cAMP dynamics are described by the FitzHugh—Nagumo model, a classical model to reproduce neuronal spiking that was previously adopted to describe excitability in *Dictyostelium* [34, 35]. Degradation of intracellular cAMP is achieved by phosphodiesterase regA, which is negatively regulated by extracellular concentration of cAMP (by means of extracellular signal—regulated kinase ERK2 [38]). Secretion of cAMP from the cell rear [38, 39] is strictly coupled to its intracellular concentration: if the extracellular cAMP concentration is below a threshold value, cells exhibit a constant small leakage of cAMP, but a temporary high concentration of cAMP is released during pulses of intracellular cAMP once above the threshold. If the extracellular cAMP concentration is kept above this threshold, the cell becomes a

sustained oscillator. Extracellular cAMP is degraded by the phosphodiesterase PDE [72]. This model correctly captures the relay of the signal and the sustained pulsing observed in *Dictyostelium* (see Supporting information for a detailed explanation).

Coarse-grained model

To reproduce the dynamics of thousands of cells, we simplified further the representation given by the detailed model. We assumed that cells are point-like objects that secrete cAMP maximally at their rear. Specifically, spatial propagation of cAMP was modeled as an exponential decay with a constant of 0.1 μm^{-1} (within a factor of 2 of the value extracted from the detailed model simulations). The spatiotemporal concentration profiles are rescaled according to the cosine of the angle with the opposite-to-motion direction; secretion becomes zero at 90˚ (lateral secretion) and is set to zero for all the frontal part of the cell. (The above-mentioned fine tuning of the exponential decay constant may be a result of this rescaling approximation or may reflect the fact that the cell—cell coupling is a key parameter for critical-like behavior.) We set a concentration threshold c_1 to determine if a given cell will emit a pulse or just leak cAMP, and a gradient threshold ∇c_2 determines if the cell will move randomly or follow the local cAMP gradient. As for the detailed model, every cell undergoes a refractory period of 6 min after firing, during which it keeps the same motion it had during pulsing. To reproduce volume exclusion, cells cannot be closer to each other than 3 μm (this rule is overwritten later in simulations, when cells are densely packed and likely superimpose). To drastically speed up simulations, the algorithm is written without explicit modeling of diffusion of cAMP in space; instead, it computes how much cAMP every cell senses and what their spatial gradients are by considering positions of cells with respect to each other. This implementation is able to reproduce aggregation of thousands of cells. More specifically, n = 1,000 cells were considered at experimental density of about one monolayer (1 ML = 6,600 cells/mm^2). For the other simulations of n = 600, 800, and 1,200, the total area (of 389 x 389 μm) was fixed and density varied accordingly. See Supporting information for a detailed explanation.

Density pair correlation

The pair-correlation function was computed as described in [73], given by

$$g(r) = \frac{A}{N(N-1)} \frac{1}{2\pi r a} \sum_{i \neq j}^{N} \delta(r - r_{ij}) \tag{3}$$

where A is the total area of the image considered, N is the number of cells, r is the radius of a ring, and a is the discretization constant. In case of a random distribution $g(r)$ takes a value of 1 on average (similar to blue trace in Fig 1D, inset ii), while in case of particle clustering, $g(r)$ becomes greater for small distances (as for the red trace in the same panel).

Spatial information

Spatial information of an image of cells was calculated in Fourier space of wave numbers based on the formalism described in [44]. All images were binarized (by means of MATLAB thresholding algorithms *graythresh* and *im2bw* for the case of experimental images). After that, 2-D images were converted in 3-D binary matrices in which the third dimension has a 1 corresponding to the pixel intensity (thus, in this case, since the starting images were binary, the 3-D matrix has a 1 at level 0 if that pixel is black and at level 1 if it is white). This guaranteed that all images had the same histogram, provided that they initially were of the same size. For the case of uncorrelated pixels, all Fourier coefficients P_i are considered independent and

Gaussian distributed. Image entropies were then calculated as:

$$H_{kS} = -2N\sum_i P_i \, log_2 \, P_i \tag{4}$$

where the probability density function P is Gaussian distributed with zero mean and variance calculated from the sum of the pixel intensities. H_{ks} is computed by dividing the function into bins of width $\sigma/100$ and summing $P_i \, log_2 \, P_i$ from -10σ to 10σ. Fourier transformation was then applied to the image. The real and imaginary part of the Fourier coefficients were then considered to compute

$$I_{kS} = \sum_i (-log_2 \, P_i^R - log_2 \, P_i^I) \tag{5}$$

where P_i^R and P_i^I refer to the real and imaginary part of coefficient i. The sum was calculated by considering bins of width $\sigma/100$ around the values assumed by the Fourier coefficients. k -space spatial information kSI was finally calculated as $kSI = H_{kS} - I_{kS}$. For a primer on information theory, see Supplementary information.

Directional correlations and susceptibility

To calculate the connected correlations, local averages of the velocities were subtracted from cell velocities. For every cell, we considered the average movement of all cells in its neighborhood up to a certain maximal distance r_c and computed the correlations between the cell in the center and all the cells belonging to its neighborhood. We repeated this procedure for every cell in our image. In this way, we were able to decrease the "bulk" velocity component in the fluctuations while keeping a continuous partition of the image (which we would have lost in case of rigid partition of the image in smaller squares) and without preassigning the final position of the aggregation center. In order to understand better the influence of this partitioning on the calculation of the connected correlations, we repeated the same procedure for different radii. Specifically, if L is the image dimension, we set r_c equal to $L/2$, $L/4$, $L/6$, $L/8$, and $L/10$, with $L/6$ appearing to be the best choice in terms of the tradeoff between avoiding overestimation of correlations and number of cells in the neighborhood for good statistics in the simulated data. For the analysis of experimental data, $L/2$, $L/3$, $L/4$, $L/5$, $L/6$, and $L/8$ were considered and $L/4$ was chosen, reflecting again the tradeoff between good statistics of a noisy dataset and a small overestimation of correlations. To plot the susceptibility, we estimated the nearest-neighbor distance, computed for every frame as the average of the nearest-neighbor distances for all cells.

Experimental methods

Time-lapse movies were obtained similar to the protocol in [22, 34]. Axenic *Dictyostelium* cells expressing the Epac1camps FRET sensor were starved for 4–5 h and then plated on hydrophobic agar for imaging. Sixteen fields of view from a microscope were combined (1.2 x 1.2 mm^2), resulting in the recording of thousands of cells in a wide field (inverted epifluorescence microscope [TE300, Nikon]). To allow high-precision tracking of individual cells in a dense cell population, a different fluorescent marker, mREPmars (TRED), was expressed and mixed with unmarked cells so a subpopulation of cells could be tracked (10% TRED cells). See Supporting information for further details.

Segmentation and tracking

Images of TRED channels were segmented by using the MATLAB function *imextendedmax*, which outputs a binary image given by the computation of the local maxima of the input

image. The centroids positions were then computed from this mask by means of the *regionprops* function. The tracking of individual cells was done by considering the centroid positions for different times. For every time t, the nearest-neighbor centroid at time $t+1$ was found, and the trajectory was accepted if the distance between the two positions was smaller than the average cell size.

Supporting information

S1 Appendix. Supporting information text. Includes detailed explanation of experimental procedure, single-cell and coarse-grained models, and experimental data analysis.
(PDF)

S1 Fig. IIllustration of spatial information. The spatial information of a hypothetical one-dimensional cell distribution (red) can be defined as the "entropy" of a maximally disordered cell distribution (even but random cell distribution in blue) minus the "entropy" of the actually peaked cell distribution (red). The more ordered (peaked or structured) the actual cell distribution, the higher the spatial information, as the entropy (uncertainty where cells are) decreases with increasing order.
(PDF)

S2 Fig. Illustration of spatial information of cells on a 2-D surface. The spatial information can be thought of as a measure of the confidence with which we can predict the presence (or absence) of a cell at a given point. Since cells are initially randomly distributed in our simulations, predicting the presence of a cell in the small light blue square in the panel on the left is much more difficult than predicting the presence of a cell in the two squares in the panel on the right.
(PDF)

S3 Fig. Compression algorithms mimic spatial information. Example of file size difference between the original JPG image and the corresponding zipped image for a coarse-grained wild-type simulation. This difference increases with cell aggregation, similar to the spatial information of the simulation shown in Fig 1F, inset ii of the main text.
(PDF)

S4 Fig. Comparison of spatial concentration profiles of secreted cAMP in detailed and coarse-grained models. Example of leaked cAMP for a detailed (A) and a coarse-grained (B) simulation. Cell shape was artificially added to an image of coarse-grained simulation in order to facilitate easier comparison (in coarse-grained simulations, cells are point-like objects with volume exclusion). cAMP secretion occurs from the rear of the cell, and in the case of the coarse-grained model, cAMP propagates more easily in the direction opposite to cell motion.
(PDF)

S5 Fig. Coarse-grained model: Cell sensing and behavior. (A) Schematic showing how cells chase each other. (B) Secretion and subsequent decision making. The behavior of cell b on the left depends on the cAMP concentration sensed and hence on the distance from the first cell (x axis) only. If the sensed concentration is above threshold c_1, cell b emits a pulse of cAMP. The spatial gradient of cAMP concentration determines the choice of movement. If the gradient is below ∇c_2, cell b chooses randomly between the two directions allowed; if instead the gradient is greater than ∇c_2, it chooses the direction that maximizes cAMP concentration.
(PDF)

S6 Fig. Schematic to explain choice of average in calculation of the connected correlations. The dashed line at the bottom of the panels represents the fact that only part of the whole image is shown. Cells *i* and *j* are moving towards the centre of aggregation, with directions u_i and u_j. (A) *U* represents the global average cell direction. δu_i and δu_j are calculated by subtracting average *U* from vectors u_i and u_j to represent fluctuations. The resulting directional correlations between *i* and *j* calculated with this procedure are greater than zero. (B) The reference direction U_i is now calculated for the neighborhood of cell *i* and is subtracted from both u_i and u_j. Fluctuations δu_i and δu_j are now correctly anticorrelated.
(PDF)

S7 Fig. Predictions from coarse-grained model. (A) Spatial information changes with *n* in in silico data. (inset) Time derivative of spatial information profiles. The change in spatial information is larger for higher cell numbers as indicated by the horizontal lines corresponding to the peak values. (B) Corresponding spatial information as a function of time for the experimental data. (inset) Similar to the simulations, the derivative tends to have higher peaks for experiments with higher cell densities, although the dark blue line does not match the trend. (C) Effect of perturbations on the system during aggregation compared to control without perturbations. A speeding up of aggregation is seen if a localized or a global, spatially uniform pulse of cAMP is given to the system during prestreaming (ps). No effect on aggregation speed is noticed if the system is perturbed during streaming (s). See S6–S9 Movies. Numerical values for simulations and experimental results are reported in S17 and S18 Data, respectively.
(PDF)

S8 Fig. Oscillations in experiments and simulations. (A) FRET signal (sum of the intensities of all pixels) in time for dataset 3. (B) Number of firing cells in time for a simulation with $n = 500$ cells. (C) Spatial propagation of cAMP pulses. The sum of the FRET signal of 100 squares is shown (see inset for the 100 regions). Data were processed with a moving average filtering for better visualization. Note secretion of cAMP corresponds to a decrease in FRET signal. Wave-like propagation of cAMP in space can clearly be seen. (D) Analysis of (C) performed on simulated data. Similar to the data, the signal propagates in space with a small delay between firing cells. Numerical data are provided in S19 Data.
(PDF)

S9 Fig. Model responses to different stimuli. (A) Detailed model responses (ii) to increasing concentrations of external cAMP (i) (amplitudes are 200, 350, and 500). (B) Response of Fitz-Hugh—Nagumo module of detailed model changes depending on the rate of external cAMP for small-amplitude (i) and large-amplitude (ii) stimulus. (C) Response of coarse-grained model to different cAMP rates for small (i) and high (ii) concentrations. Numerical data are provided in S20 Data.
(PDF)

S10 Fig. Estimation of total numbers of cells. (A) Number of TRED cells, estimated by segmentation. In order to avoid boundary artifacts, a fraction of the field of cells was imaged. This implies that during aggregation, the number of cells increases because of movement towards the aggregation center. In particular, the number of cells increases during streaming (while after aggregation the number decreases again because of difficulty in following individual cells). (B) Fraction of TRED cells with respect to total cells for the first 100 min. Numerical data are provided in S21 Data.
(PDF)

S11 Fig. Further support for critical-like behavior in the data. (A) Cell speed during aggregation. Speed was estimated from the average cell movement from frame to frame. (B) Speed-FRET oscillations. A moving average filter was applied to the two signals, which were subsequently normalized for comparison. (C) Distributions of directions. The different angles of directional fluctuations were collected for 50 frames (see color bar in panel A for corresponding times) and plotted as a distribution. The red lines represent the fits to the von Mises distribution. Underneath the plots, the results of a two-sample Kolmogorov—Smirnov test performed with MATLAB *kstest2* function and corresponding p -values are reported. $H = 0$ ($H = 1$) indicates that the null hypothesis of identical distributions cannot (can be) rejected. (D) Cluster-size distribution for different time points. (top) Cell directions. Squares represent the angles of movement of individual cells. (bottom) Corresponding cluster-size distributions. Numerical data are provided in zipped folder S22 Data.
(PDF)

S12 Fig. Connected correlations for cell direction (top) and speed (bottom). Connected correlations increase with similar amplitudes and timings for direction (already presented and described in the main text) and speed. Numerical data are provided in S13 Data.
(PDF)

S13 Fig. Autocorrelation profiles for wild-type and mutant data. Autocorrelations (solid lines) and corresponding fits (dashed lines) for the left panels of Fig 5A–C in [55]. Numerical data are provided in S16 Data.
(PDF)

S1 Table. Parameter values for detailed model. Space and time units were set according to the diffusion constant of cAMP, and are respectively μm and s for every parameter. Concentration is instead in arbitrary units but can be chosen of order μM for the intracellular and nM for extracellular cAMP [22].
(PDF)

S1 Movie. Single-cell model: Streaming. Single cell in a box with a periodic boundary to simulate streaming. Because of the rectangular box elongated in the vertical direction, the cell can sense its own secretion when moving in the horizontal direction but not when moving in the vertical direction. See Fig 1B of the main text for more details.
(AVI)

S2 Movie. Single-cell model: Wave response. Single cell in a box to simulate the response to an external wave of cAMP. The wave moves from right to left, and the cell consequently moves from left to right towards the incoming wave. See Fig 1C of the main text for more details.
(AVI)

S3 Movie. Single-cell model: Aggregation. Four cells in a box to simulate aggregation. One cell can pulse while the others just leak cAMP. Cells tend to cluster, mimicking small-scale aggregation. See Fig 1D of the main text for more details.
(AVI)

S4 Movie. Coarse-grained simulations. $n = 1{,}000$ cells, simulated for about 330 min, as shown in Figs 1F and 2 of the main text. At the beginning of the simulation, cells are just secreting a small amount of cAMP. Because of their random movement, cells come close to each other and thus can sense a larger-than-threshold concentration of cAMP. This causes the cells to fire, resulting in wave propagation and cell aggregation.
(AVI)

S5 Movie. Experimental movie. Dataset 3, shown in Fig 3 of the main text. See Materials and methods and Supporting information for experimental details.
(MP4)

S6 Movie. Global perturbation during prestreaming for coarse-grained simulations. n = 1,000 cells, simulated for about 330 min; see S7 Fig in Supporting information for details. An external uniform concentration of cAMP is applied before the streaming phase, causing a speed-up of aggregation. The time point of the addition of cAMP is represented by a yellow asterisk.
(AVI)

S7 Movie. Global perturbation during streaming for coarse-grained simulations. n = 1,000 cells, simulated for about 330 min; see S7 Fig in Supporting information for details. An external uniform concentration of cAMP is applied to all cells during the streaming phase, with no apparent effect on the aggregation dynamics. The time point of the addition of cAMP is represented by a yellow asterisk.
(AVI)

S8 Movie. Local perturbation during prestreaming for coarse-grained simulations. n = 1,000 cells, simulated for about 330 min; see S7 Fig in Supporting information for details. An external point-like concentration of cAMP is applied before the streaming phase, causing a speed-up of aggregation and steering of the cells towards the location of the cAMP. The time point and the location of the added cAMP are represented by yellow asterisks.
(AVI)

S9 Movie. Local perturbation during streaming for coarse-grained simulations. n = 1,000 cells, simulated for about 330 min; see S7 Fig in Supporting information for details. An external point-like concentration of cAMP is applied during the streaming phase. Opposite to what happens for point-like stimulations prior to the streaming phase, this later stimulation seems to have little effect on aggregation dynamics. However, the location of the aggregation center is influenced by the cAMP. The time point and the location of the added cAMP are represented by yellow asterisks.
(AVI)

S10 Movie. Coarse-grained simulations of wild-type cells. n = 500 cells, simulated for about 660 min (to allow for complete aggregation); see Fig 4 of the main text for details. These simulations reflect the ones shown in S4 Movie but with fewer cells to allow for the comparison with the mutant S11–S14 Movies.
(AVI)

S11 Movie. Coarse-grained simulations for radially symmetric secretion of cAMP. n = 500 cells, simulated for about 330 min; see Fig 4 of the main text for details. Cells are not capable of aggregating if the release of cAMP (leakage and pulses) is radially symmetric.
(AVI)

S12 Movie. Coarse-grained simulations for increased cell-sensing noise. n = 500 cells, simulated for about 330 min; see Fig 4 of the main text for details. Coarse-grained simulations are quite robust to increased sensing noise, with cells still capable to aggregate.
(AVI)

S13 Movie. Coarse-grained simulations for added cell—cell adhesion. n = 500 cells, simulated for about 330 min; see Fig 4 of the main text for details. When cells are attracted to each other because of the adhesive force, they are no longer capable of coherent streaming and

hence aggregation, forming multiple clusters instead.
(AVI)

S14 Movie. Coarse-grained simulations for random refractory periods. n = 500 cells, simulated for about 330 min; see Fig 4 of the main text for details. Cells which do not fire synchronously cannot communicate effectively and consequently aggregate incompletely into multiple clusters.
(AVI)

S1 Data. Detailed model data. Detailed model data for results shown in Fig 1. The same simulations capturing streaming, wave response and aggregation were repeated 12 times.
(MAT)

S2 Data. Detailed model code. Java code to run detailed model (in a zipped folder). The user needs to create a folder called simulations in their home directory. After that, run the code and retrieve.txt files containing cell position (relative to the box and "absolute," i.e., without accounting for periodic boundary conditions) and concentration values for internal chemistry.
(ZIP)

S3 Data. Spatial information comparison between model and experimental data. Data have been shifted and normalised for comparison. For unscaled data, see S18 Data for spatial information of experimental data and S17 Data for simulation results.
(MAT)

S4 Data. Code for coarse-grained model. MATLAB code (in a zipped folder) written to simulate aggregation of coarse-grained cells. Includes *cell_secretion.mat* with concentration profiles of cell secretion needed as input.
(ZIP)

S5 Data. Data for coarse-grained simulations correlation analysis. Contains correlation time values for simulated data, with radius equal to $L/2$, $L/4$, $L/6$, $L/8$, and $L/10$. Number of cells n is 600, 800, 1000, and 1,200. All data presented in Fig 2 are stored. Here, $x0$ refers to correlation length and *chi* to susceptibility.
(MAT)

S6 Data. Cell positions and tracking for experimental movie with n = 1,040 cells. Each data cell represents one time frame, and contains a matrix with four columns: x and y coordinates of cell at time t and x' and y' coordinates of cell at time $t + 1$.
(MAT)

S7 Data. Cell positions and tracking for experimental movie with n = 950 cells. Each data cell represents one time frame and contains a matrix with four columns: x and y coordinates of cell at time t and x' and y' coordinates of cell at time $t + 1$.
(MAT)

S8 Data. Cell positions and tracking for experimental movie with n = 800 cells. Each data cell represents one time frame and contains a matrix with four columns: x and y coordinates of cell at time t and x' and y' coordinates of cell at time $t + 1$.
(MAT)

S9 Data. Cell positions and tracking for experimental movie with n = 480 cells. Each data cell represents one time frame, and contains a matrix with four columns: x and y coordinates of cell at time t and x' and y' coordinates of cell at time $t + 1$.
(MAT)

S10 Data. Cell positions and tracking for experimental movie with $n = 360$ cells. Each data cell represents one time frame and contains a matrix with four columns: x and y coordinates of cell at time t and x' and y' coordinates of cell at time $t + 1$.
(MAT)

S11 Data. Cell positions and tracking for experimental movie with $n = 350$ cells. Each data cell represents one time frame and contains a matrix with four columns: x and y coordinates of cell at time t and x' and y' coordinates of cell at time $t + 1$.
(MAT)

S12 Data. Spatial information and susceptibility for experimental data. Results are shown in Fig 3C.
(MAT)

S13 Data. Correlation analysis for experimental data. Results are shown in Fig 3D–3F and S12 Fig. Contains correlation values for all experimental movies, together with correlation length and susceptibility ("chi"). Also includes numerical values for speed correlation of dataset 3, shown in S12 Fig.
(MAT)

S14 Data. Correlation length versus neighborhood radius for experimental data. Results are shown in Fig 3G. Contains correlation length with different neighborhood radii for all experimental movies ($L/2$, $L/3$, $L/4$, $L/5$, $L/6$, $L/8$).
(MAT)

S15 Data. Correlations and spatial information for mutant simulations. Results are shown in Fig 4A. Contains correlation lengths ($x0$) and spatial information profiles (kSI) for simulations of WT ("nomod"), uniform secretion ("uniformsec"), sensing noise ("tennoise"), cell—cell adhesion ("lj"), and asynchronous secretion ("randref").
(MAT)

S16 Data. Correlations and spatial information for mutant experiments. Contains autocorrelation values and fit parameters, together with spatial information results for mutant data, shown in Fig 4B and S13 Fig.
(MAT)

S17 Data. Spatial information time profiles for coarse-grained simulations. Numerical values for spatial information for number of cells n = 600, 800, 1,000, and 1,200, shown in S7A Fig. Also includes values for perturbated simulations shown in S7C Fig.
(MAT)

S18 Data. Spatial information time profiles for experimental data. Results are shown in S7B Fig.
(MAT)

S19 Data. FRET propagation for simulated and experimental data. Includes 'global' signals of S8 Fig, panels A and B and "local" signals of panels C and D, together with the processed signal values that are actually showed in the image.
(MAT)

S20 Data. Detailed and coarse-grained model responses to external cAMP stimuli. Results are shown in S9 Fig.
(MAT)

S21 Data. Number of cells and TRED ratio comparison between experimental datasets. Results are shown in S10 Fig.
(MAT)

S22 Data. Critical-like behavior in experimental data. Zipped folder including numerical values for S11 Fig. Includes FRET and speed signals, angle values for histograms of panel C, and cluster size distributions of panel D.
(ZIP)

Acknowledgments

We are grateful to the Gregor lab at Princeton University for sharing their data with us and additionally to Thomas Gregor, Allyson Sgro, and Monika Skoge for helpful discussions and comments on the manuscript. We also thank Luke Tweedy for help with the detailed model, Javier López-Garrido and Linus Schumacher for a critical reading of the manuscript, and Mariam Elgabry and Suhail Islam for support with computational issues.

Author Contributions

Conceptualization: GDP, RGE.

Data curation: GDP, DY.

Formal analysis: GDP, RGE.

Funding acquisition: RGE.

Investigation: GDP, DY.

Methodology: GDP, RGE.

Project administration: RGE.

Resources: DY, RGE.

Software: GDP.

Supervision: RGE.

Validation: GDP, RGE, DY.

Visualization: GDP, RGE.

Writing – original draft: GDP, RGE.

Writing – review & editing: GDP, RGE, DY.

References

1. Sumpter D, Buhl J, Biro D, Couzin I. Information transfer in moving animal groups. Theory in Biosciences. 2008; 127(2):177–186. https://doi.org/10.1007/s12064-008-0040-1 PMID: 18458976
2. Vicsek T, Zafeiris A. Collective motion. Physics Reports. 2012; 517(3–4):71–140. http://dx.doi.org/10.1016/j.physrep.2012.03.004.
3. Mehes E, Vicsek T. Collective motion of cells: from experiments to models. Integrative Biology. 2014; 6:831–854. https://doi.org/10.1039/c4ib00115j PMID: 25056221
4. Ashe HL, Briscoe J. The interpretation of morphogen gradients. Development. 2006; 133(3):385–394. https://doi.org/10.1242/dev.02238 PMID: 16410409

5. Morrison AH, Scheeler M, Dubuis J, Gregor T. Quantifying the Bicoid Morphogen Gradient in Living Fly Embryos. Cold Spring Harbor Protocols. 2012; 2012(4):398–406. https://doi.org/10.1101/pdb.top068536 PMID: 22474658
6. van den Brink SC, Baillie-Johnson P, Balayo T, Hadjantonakis AK, Nowotschin S, Turner DA, et al. Symmetry breaking, germ layer specification and axial organisation in aggregates of mouse embryonic stem cells. Development. 2014; 141(22):4231–4242. https://doi.org/10.1242/dev.113001 PMID: 25371360
7. Kaliman S, Jayachandran C, Rehfeldt F, Smith AS. Novel growth regime of MDCK II model tissues on soft substrates. Biophysical Journal. 2014; 106(7):L25 –L28. http://dx.doi.org/10.1016/j.bpj.2013.12.056. PMID: 24703316
8. Attanasi A, Cavagna A, Del Castello L, Giardina I, Melillo S, Parisi L, et al. Finite-size scaling as a way to probe near-criticality in natural swarms. Physical Review Letters. 2014; 113:238102. https://doi.org/10.1103/PhysRevLett.113.238102 PMID: 25526161
9. Cavagna A, Cimarelli A, Giardina I, Parisi G, Santagati R, Stefanini F, et al. Scale-free correlations in starling flocks. Proceedings of the National Academy of Sciences. 2010; 107(26):11865–11870.
10. Chialvo DR. Emergent complex neural dynamics. Nature Physics. 2010; 6(10):744–750.
11. Levine H, Rappel WJ. The physics of eukaryotic chemotaxis. Physics Today. 2013; 66(2):24–30. http://dx.doi.org/10.1063/PT.3.1884.
12. Bretschneider T, Jonkman J, Köhler J, Medalia O, Barisic K, Weber I, et al. Dynamic organization of the actin system in the motile cells of Dictyostelium. Journal of Muscle Research & Cell Motility. 2002; 23 (7):639–649.
13. Devreotes P. Dictyostelium discoideum: a model system for cell-cell interactions in development. Science. 1989; 245(4922):1054–1058. PMID: 2672337
14. Gerisch G. Cell aggregation and differentiation in *Dictyostelium*. Current Topics in Developmental Biology. 1968; 3:157. PMID: 5002049
15. Rietdorf J, Siegert F, Weijer CJ. Induction of optical density waves and chemotactic cell movement in dictyostelium discoideum by microinjection of cAMP pulses. Developmental Biology. 1998; 204(2):525–536. http://dx.doi.org/10.1006/dbio.1998.9088. PMID: 9882487
16. Weijer CJ. Morphogenetic cell movement in Dictyostelium. Seminars in Cell & Developmental Biology. 1999; 10(6):609–619. http://dx.doi.org/10.1006/scdb.1999.0344.
17. Alcantara F, Monk M. Signal propagation during aggregation in the slime mold *Dictyostelium discoideum*. Journal of General Microbiology. 1974; 85:321. https://doi.org/10.1099/00221287-85-2-321 PMID: 4615133
18. Gross JD, Peacey MJ, Trevan DJ. Signal emission and signal propagation during early aggregation in Dictyostelium discoideum. Journal of Cell Science. 1976; 22(3):645–656. PMID: 1035221
19. Tomchik K, Devreotes P. Adenosine 3',5'-monophosphate waves in Dictyostelium discoideum: a demonstration by isotope dilution—fluorography. Science. 1981; 212(4493):443–446. PMID: 6259734
20. Martiel JL, Goldbeter A. A model based on receptor desensitization for cyclic AMP signaling in Dictyostelium cells. Biophysical Journal. 1987; 52(5):807–828. http://dx.doi.org/10.1016/S0006-3495(87)83275-7. PMID: 19431710
21. Sawai S, Thomason PA, Cox EC. An autoregulatory circuit for long-range self-organization in *Dictyostelium* cell populations. Nature. 2005; 433:323. https://doi.org/10.1038/nature03228 PMID: 15662425
22. Gregor T, Fujimoto K, Masaki N, Sawai S. The onset of collective behavior in social amoebae. Science. 2010; 328(5981):1021–1025. https://doi.org/10.1126/science.1183415 PMID: 20413456
23. Skoge M, Yue H, Erickstad M, Bae A, Levine H, Groisman A, et al. Cellular memory in eukaryotic chemotaxis. Proceedings of the National Academy of Sciences. 2014; 111(40):14448–14453.
24. Nakajima A, Ishihara S, Imoto D, Sawai S. Rectified directional sensing in long-range cell migration. Nature Communications. 2014; 5:5367. https://doi.org/10.1038/ncomms6367 PMID: 25373620
25. Tweedy L, Meier B, Stephan J, Heinrich D, Endres RG. Distinct cell shapes determine accurate chemotaxis. Scientific Reports. 2013; 3:2606. https://doi.org/10.1038/srep02606 PMID: 24008441
26. Meinhardt H. Orientation of chemotactic cells and growth cones: models and mechanisms. Journal of Cell Science. 1999; 112(17):2867–2874.
27. Parent CA, Devreotes PN. A Cell's Sense of Direction. Science. 1999; 284(5415):765–770. PMID: 10221901
28. Levchenko A, Iglesias PA. Models of Eukaryotic Gradient Sensing: Application to Chemotaxis of Amoebae and Neutrophils. Biophysical Journal. 2002; 82(1):50–63. http://dx.doi.org/10.1016/S0006-3495(02)75373-3.

29. Kessler DA, Levine H. Pattern formation in *Dictyostelium* via the dynamics of cooperative biological entities. Physical Review E. 1993; 48:4801–4804.

30. Levine H. Modeling spatial patterns in Dictyostelium. Chaos. 1994; 4(3):563–568. http://dx.doi.org/10.1063/1.166050. PMID: 12780133

31. Levine H, Aranson I, Tsimring L, Truong TV. Positive genetic feedback governs cAMP spiral wave formation in Dictyostelium. Proceedings of the National Academy of Sciences. 1996; 93(13):6382–6386.

32. Maini PK, Woolley TE, Baker RE, Gaffney EA, Lee SS. Turing's model for biological pattern formation and the robustness problem. Interface Focus. 2012; 2(4):487–496. https://doi.org/10.1098/rsfs.2011.0113 PMID: 23919129

33. Umulis DM, Othmer HG. Mechanisms of scaling in pattern formation. Development. 2013; 140 (24):4830–4843. https://doi.org/10.1242/dev.100511 PMID: 24301464

34. Sgro AE, Schwab DJ, Noorbakhsh J, Mestler T, Mehta P, Gregor T. From intracellular signaling to population oscillations: bridging size- and time-scales in collective behavior. Molecular Systems Biology. 2015; 11(1):779. https://doi.org/10.15252/msb.20145352 PMID: 25617347

35. Noorbakhsh J, Schwab DJ, Sgro AE, Gregor T, Mehta P. Modeling oscillations and spiral waves in *Dictyostelium* populations. Physical Review E. 2015; 91:062711.

36. Gao T, Roisin-Bouffay C, Hatton RD, Tang L, Brock DA, DeShazo T, et al. A Cell Number-Counting Factor Regulates Levels of a Novel Protein, SslA, as Part of a Group Size Regulation Mechanism in Dictyostelium. Eukaryotic Cell. 2007; 6(9):1538–1551. https://doi.org/10.1128/EC.00169-07 PMID: 17660362

37. Neilson MP, Veltman DM, van Haastert PJM, Webb SD, Mackenzie JA, Insall RH. Chemotaxis: A Feedback-Based Computational Model Robustly Predicts Multiple Aspects of Real Cell Behaviour. PLoS Biol. 2011; 9(5):e1000618. https://doi.org/10.1371/journal.pbio.1000618 PMID: 21610858

38. McMains VC, Liao X, Kimmel AR. Oscillatory signaling and network responses during the development of *Dictyostelium discoideum*. Ageing Research Reviews. 2008; 7(3):234–48. https://doi.org/10.1016/j.arr.2008.04.003 PMID: 18657484

39. Kriebel PW, Barr VA, Rericha EC, Zhang G, Parent CA. Collective cell migration requires vesicular trafficking for chemoattractant delivery at the trailing edge. The Journal of Cell Biology. 2008; 183(5):949–961. https://doi.org/10.1083/jcb.200808105 PMID: 19047467

40. Tyson JJ, Murray JD. Cyclic AMP waves during aggregation of Dictyostelium amoebae. Development. 1989; 106(3):421–426. PMID: 2557197

41. Van Haastert PJM. A stochastic model for chemotaxis based on the ordered extension of pseudopods. Biophysical Journal. 2010; 99(10):3345–3354. https://doi.org/10.1016/j.bpj.2010.09.042 PMID: 21081083

42. Samadani A, Mettetal J, van Oudenaarden A. Cellular asymmetry and individuality in directional sensing. Proceedings of the National Academy of Sciences. 2006; 103:11549.

43. Cooper R, Wingreen NS, Cox EC. An excitable cortex and memory model successfully predicts new pseudopod dynamics. PLoS ONE. 2012; 7:e33528. https://doi.org/10.1371/journal.pone.0033528 PMID: 22457772

44. Heinz W, Werbin J, Lattman E, Hoh J. Computing Spatial Information from Fourier Coefficient Distributions. The Journal of Membrane Biology. 2011; 241(2):59–68. https://doi.org/10.1007/s00232-011-9362-x PMID: 21544539

45. Jensen HJ. Self-organized criticality. Cambridge University Press; 1998.

46. Palsson E, Othmer HG. A model for individual and collective cell movement in *Dictyostelium discoideum*. Proceedings of the National Academy of Sciences. 2000; 97(19):10448–10453.

47. Toner J, Tu Y. Flocks, herds, and schools: A quantitative theory of flocking. Physical Review E. 1998; 58:4828–4858.

48. Toner J. Reanalysis of the hydrodynamic theory of fluid, polar-ordered flocks. Physical Review E. 2012; 86:031918.

49. Machta B, Chachra R, Transtrum M, Sethna J. Parameter space compression underlies emergent theories and predictive models. Science. 2013; 342:604. https://doi.org/10.1126/science.1238723 PMID: 24179222

50. Loomis W. Genetic control of morphogenesis in *Dictyostelium*. Developmental Biology. 2015; 402:146. https://doi.org/10.1016/j.ydbio.2015.03.016 PMID: 25872182

51. Abe K, Yanagisawa K. A new class of rapidly developing mutants in *Dictyostelium discoideum*: implications for cyclic AMP metabolism and cell differentiation. Developmental Biology. 1983; 95:200. PMID: 6298035

52. Chang WT, Thomason PA, Gross JD, Newell PC. Evidence that the RdeA protein is a component of a multistep phosphorelay modulating rate of development in Dictyostelium. The EMBO Journal. 1998; 17 (10):2809–2816. https://doi.org/10.1093/emboj/17.10.2809 PMID: 9582274

53. Thomason P, Traynor D, Cavet G, Chang W, Harwood A, Kay R. An intersection of the cAMP/PKA and two-component signal transduction systems in Dictyostelium. The EMBO Journal. 1998; 17:2838. https://doi.org/10.1093/emboj/17.10.2838 PMID: 9582277

54. Brown J, Firtel R. Just the right size: cell counting in *Dictyostelium*. Trends in Genetics. 2000; 16:191. PMID: 10782107

55. Sawai S, Guan X, Kuspa A, Cox E. High-throughput analysis of spatio-temporal dynamics in *Dictyostelium*. Genome Biology. 2007; 8:R144. https://doi.org/10.1186/gb-2007-8-7-r144 PMID: 17659086

56. Okuwa T, Katayama T, Takano A, Kodaira K, Yasukawa H. Two cell-counting factors regulate the aggregate size of the cellular slime mold *Dictyostelium discoideum*. Development, Growth & Differentiation. 2001; 43:735.

57. Dallon JC, Dalton B, Malani C. Understanding Streaming in Dictyostelium discoideum: Theory Versus Experiments. Bulletin of Mathematical Biology. 2011; 73(7):1603–1626. https://doi.org/10.1007/s11538-010-9583-7 PMID: 20936368

58. Tweedy L, Knecht DA, Mackay GM, Insall RH. Self-Generated Chemoattractant Gradients: Attractant Depletion Extends the Range and Robustness of Chemotaxis. PLoS Biol. 2016; 14(3):1–22.

59. Kriebel P, Barr V, Parent C. Adenylyl cyclase localization regulates streaming during chemotaxis. Cell. 2003; 112:549. PMID: 12600317

60. Cohen M, Robertson A. Wave propagation in the early stages of aggregation of cellular slime molds. Journal of Theoretical Biology. 1971; 31:101. PMID: 4325172

61. Cohen M, Robertson A. Chemotaxis and the early stages of aggregation in cellular slime molds. Journal of Theoretical Biology. 1971; 31:119. PMID: 4325173

62. Bhowmik A, Rappel WJ, Levine H. Excitable waves and direction-sensing in Dictyostelium discoideum: steps towards a chemotaxis model. Physical Biology. 2016; 13(1):016002. https://doi.org/10.1088/1478-3975/13/1/016002 PMID: 26824302

63. Hashimoto Y, Cohen M, Robertson A. Cell density dependence of the aggregation characteristics of the cellular slime mould *Dictyostelium discoideum*. Journal of Cell Science. 1975; 19:215. PMID: 1236856

64. Mermin ND, Wagner H. Absence of Ferromagnetism or Antiferromagnetism in One- or Two-Dimensional Isotropic Heisenberg Models. Physical Review Letters. 1966; 17:1133–1136.

65. Kosterlitz JM, Thouless DJ. Ordering, metastability and phase transitions in two-dimensional systems. Journal of Physics C: Solid State Physics. 1973; 6(7):1181.

66. Moretti P, Muñoz MA. Griffiths phases and the stretching of criticality in brain networks. Nature Communications. 2013; 4:2521. https://doi.org/10.1038/ncomms3521 PMID: 24088740

67. Krotov D, Dubuis JO, Gregor T, Bialek W. Morphogenesis at criticality. Proceedings of the National Academy of Sciences. 2014; 111(10):3683–3688.

68. Vicsek T, Czirók A, Ben-Jacob E, Cohen I, Shochet O. Novel Type of Phase Transition in a System of Self-Driven Particles. Physical Review Letters. 1995; 75:1226–1229. https://doi.org/10.1103/PhysRevLett.75.1226 PMID: 10060237

69. Nagy M, Akos Z, Biro D, Vicsek T. Hierarchical group dynamics in pigeon flocks. Nature. 2010; 464 (7290):890–893. https://doi.org/10.1038/nature08891 PMID: 20376149

70. Bialek W, Cavagna A, Giardina I, Mora T, Silvestri E, Viale M, et al. Statistical mechanics for natural flocks of birds. Proceedings of the National Academy of Sciences. 2012; 109(13):4786–4791.

71. Prindle A, Liu J, Asally M, Ly S, Garcia-Ojalvo J, Suel GM. Ion channels enable electrical communication in bacterial communities. Nature. 2015; 527(7576):59–63. https://doi.org/10.1038/nature15709 PMID: 26503040

72. Bader S, Kortholt A, Van Haastert PJM. Seven Dictyostelium discoideum phosphodiesterases degrade three pools of cAMP and cGMP. Biochemical Journal. 2007; 402(1):153–161. https://doi.org/10.1042/BJ20061153 PMID: 17040207

73. Gurry T, Kahramanoğulları O, Endres RG. Biophysical Mechanism for Ras-Nanocluster Formation and Signaling in Plasma Membrane. PLoS ONE. 2009; 4(7):e6148. https://doi.org/10.1371/journal.pone.0006148 PMID: 19587789